Check for updates

Advanced Functional Materials

ADVANCED FUNCTIONAL MATERIALS
www.afm-journal.de

RESEARCH ARTICLE

Wake-Induced Vibration Enhanced Triboelectric Nanogenerator for Efficient Energy Harvesting From Low-Velocity Water Flows and Self-Powered Sensing

Xinyu Zhang[1] | Zeye Sun[1] | Yawei Wang[2] | Yizhou Li[2] | Guobiao Hu[2] | Junlei Wang[1] | Xianhu Liu[3] | Caofeng Pan[4]

[1]School of Mechanical and Power Engineering, Zhengzhou University, Zhengzhou, China | [2]Internet of Things Thrust, The Hong Kong University of Science and Technology (Guangzhou), Guangzhou, China | [3]State Key Laboratory of Structural Analysis, Optimization and CAE Software for Industrial Equipment, Zhengzhou University, Zhengzhou, China | [4]Beijing Key Laboratory for Atomic Manufacturing Equipment and Intelligent Sensing, Institute of Atomic Manufacturing, Beihang University, Beijing, China

Correspondence: Junlei Wang (jlwang@zzu.edu.cn) | Xianhu Liu (xianhu.liu@zzu.edu.cn) | Caofeng Pan (pancaofeng@buaa.edu.cn)

Received: 18 March 2026 | **Revised:** 1 July 2026 | **Accepted:** 22 July 2026

Keywords: energy harvesting | low-velocity water flow | self-powered sensing | triboelectric nanogenerator | wake-induced vibration

ABSTRACT

Low-velocity water flows (<0.5 m s^{-1}) remain largely underutilized due to the poor adaptability and high cut-in thresholds of conventional generators. To address this limitation and fulfil the self-powering demands of distributed sensors for river ecosystem monitoring, we report a **wake-induced vibration triboelectric nanogenerator (W-TENG)** that leverages flow-induced instabilities for energy harvesting. By introducing an upstream bluff body, periodic vortex shedding is harnessed to amplify oscillation amplitude and contact frequency, thereby enhancing triboelectric charge generation. Systematic structural optimization and performance evaluation reveal the W-TENG's remarkable adaptability to low-speed aquatic environments, achieving an ultralow cut-in velocity of **0.15** m s^{-1} and a peak volumetric power density of 18.26 W m^{-3} at 0.4 m s^{-1}. To enhance energy conversion efficiency, an integrated energy management circuit is developed, enabling a 6.13-fold increase in capacitor charging rate. As a proof-of-concept, the harvested energy is successfully used to power a wireless temperature sensor, enabling real-time environmental data transmission to a mobile device without external power input. This work provides a practical and scalable approach for harvesting energy from water flows at low velocities and developing self-powered sensing systems for river ecological monitoring.

1 | Introduction

Rivers constitute a vital water resource for domestic and industrial consumption, agricultural irrigation, and manufacturing processes, thereby underpinning the development of human civilizations [1–5]. Effective monitoring of river ecosystems is of paramount importance [6–8]. With the advancement of Internet of Things (IoT) technologies, sensors have been widely adopted in fields such as smart agriculture, environmental monitoring, and telecommunications, making them an effective tool for river ecosystem surveillance [9–11]. The widespread deployment of such sensors has led to a substantial increase in the demand for reliable power sources [12–14]. Batteries are currently the widely adopted solution; however, their limited capacity and

Xinyu Zhang, Zeye Sun and Yawei Wang contributed equally to this work.

All rights reserved, including rights for text and data mining and training of artificial intelligence technologies or similar technologies.
© 2026 Wiley-VCH GmbH

potential environmental pollution pose significant challenges [15]. In this regard, harvesting sustainable energy directly from the ambient environment has become increasingly attractive [16]. However, the generally low flow velocity in most rivers (typically below 1 m s^{-1}), together with pronounced spatial variability, severely constrains efficient energy utilization [17]. Conventional electromagnetic generators (EMGs), which are widely employed for large-scale grid power generation, suffer from high fabrication costs, potential ecological disturbance, and difficulty in initiating operation under low-flow conditions [18–20]. These limitations highlight the need for alternative energy-harvesting strategies.

In recent years, rapid advances in science and technology have driven the emergence of various novel energy harvesting approaches [21, 22]. Among them, triboelectric nanogenerator (TENG) technology, which is based on the coupled effects of contact electrification (or triboelectrification) and electrostatic induction, has attracted considerable attention from the academic community [23–26]. TENGs offer several advantages, including broad material availability, high environmental adaptability, simple fabrication processes, and low manufacturing costs, and they demonstrate favorable output performance under low-flow-velocity conditions [27, 28]. Quantitative methods, such as the kinetic energy calculation and current integration (KECCI) method proposed by Zheng et al. [29], have also been developed to analyze the mechanical-to-electrical energy conversion process in TENG systems. However, most existing designs rely on passive flow excitation, limiting their ability to effectively harness low-intensity hydrodynamic energy.

For river environments with relatively low flow velocities, TENG devices have been developed in diverse configurations. Jin et al. designed a double helix rotating triboelectric nanogenerator (DHR-TENG) capable of achieving a performance output at a flow velocity of 0.8 m s^{-1} [30]. Jing et al. designed a 3D fully-enclosed bionic fish-body structure, achieving an output of 7 W m^{-3} at a flow velocity of 0.81 m s^{-1} [31]. Although these studies have reduced the operational flow velocity of TENG devices, their peak output performance still requires flow velocities close to 1 m s^{-1}. To enhance the overall operational range of the device, Li et al. proposed a hybrid design combining EMG and TENG, enabling stage-based power generation across varying flow velocities and significantly expanding the energy harvesting range [32]. However, this water wheel-based design is highly susceptible to environmental interference; for instance, the device is prone to entanglement by aquatic plants, and its blades are easily damaged by water flow impact. Additionally, the flag-shaped TENG possesses high sensitivity to flow disturbance, making it suitable for harvesting water flow energy at low velocities. For example, Huang et al. designed an underwater flag-shaped TENG that initiates operation at an ultra-low flow velocity of 0.02 m s^{-1}. [33] However, this type of underwater flag-shaped TENG imposes stringent requirements on device waterproofing and corrosion resistance.

Flow-induced vibration (FIV) is a common phenomenon in underwater energy harvesting systems [34, 35]. It refers to the periodic or random vibration of an object induced by flow instability when fluid passes over it [36]. Fundamentally, FIV arises from the coupling between fluid dynamic forces and the elastic–inertial response of the structure. Depending on the excitation mechanism, FIV can be broadly categorized into vortex-induced vibration (VIV), galloping, flutter, and related modes [37–39]. Although FIV is often regarded as a factor that may adversely affect device stability and output performance, increasing attention has been directed toward its potential for harvesting water flow energy under low-velocity conditions. For instance, Zhang et al. inspired by a fish tail, designed a bionic-fish-tail TENG driven by the FIV effect, achieving an output power density of 5.567 W m^{-3} at a flow velocity of 0.89 m s^{-1} [40]. In another study, Wang et al. utilized a cylinder-induced vortex street to drive a flag-shaped TENG, which initiated operation at a flow velocity as low as 0.133 m s^{-1} [41]. This mode features a low cut-in flow velocity by directly converting the vortex-induced flutter of a flexible flag into triboelectric output. To enhance energy harvesting performance, numerous studies have sought to increase the vibration response of flow-induced energy harvesters through optimization of bluff body geometry and structural parameters [42]. Recent studies on wake-induced vibration (WIV) energy harvesters have shown that tandem bluff body configurations can enhance the vibration response of the downstream bluff body through wake interaction [43–45]. WIV is driven by unsteady vortex-structure interactions between the upstream wake and the downstream body. Coherent wake vortices induce fluctuating fluid forces, and a favorable phase lag between displacement and fluid force enables positive energy transfer from the flow to the structure, thereby sustaining oscillation [46]. Compared with conventional VIV systems that rely on synchronization within a limited lock-in region, WIV can maintain effective excitation over a broader range of flow conditions [47–49].

Despite recent advances, a general strategy that simultaneously lowers the cut-in flow velocity, enhances energy conversion efficiency, and maintains structural robustness remains lacking. Based on the aforementioned challenges and prior studies, this work proposes a wake-induced vibration triboelectric nanogenerator (W-TENG) for harvesting energy from shallow water flows with low velocities. The W-TENG features a simple and modular architecture with stackable TENG units and a fully encapsulated housing to minimize environmental interference. In contrast to previously reported flexible flag-like, fin-like, or rotating TENG designs, the proposed W-TENG converts the wake-induced oscillation of the downstream bluff body into bearing-supported swinging of the TENG module, which drives gravity-induced rolling contact within the stacked units. Meanwhile, the TENG module remains above the water surface while the bluff bodies interact with the flow, thereby reducing direct water exposure. A multi-dimensional optimization framework-integrating theoretical modeling, parametric simulation, and experimental validation-was adopted to identify the optimal device parameters. Performance evaluations under different flow velocities demonstrate that the device can initiate stable operation at 0.15 m s^{-1}. At a flow velocity of 0.4 m s^{-1}, it delivers a peak output voltage of 278.55 V, a current of 2.52 μA, a transferred charge of 209.7 nC, and a maximum volumetric power density of 18.26 W m^{-3}. These results demonstrate a clear improvement in output performance compared with previously reported devices, while simultaneously lowering the minimum operational flow velocity. By incorporating a tailored energy management circuit, the W-TENG's capacitor charging rate was increased several-fold, allowing it to continuously power an electronic timer. Moreover, a fully self-powered wireless temperature sensor was developed,

16163028, 2026, 71, Downloaded from https://advanced.onlinelibrary.wiley.com/doi/10.1002/adfm.77518 by Beihang University (Buaa), Wiley Online Library on [23/09/2026]. See the Terms and Conditions (https://onlinelibrary.wiley.com/terms-and-conditions) on Wiley Online Library for rules of use; OA articles are governed by the applicable Creative Commons License

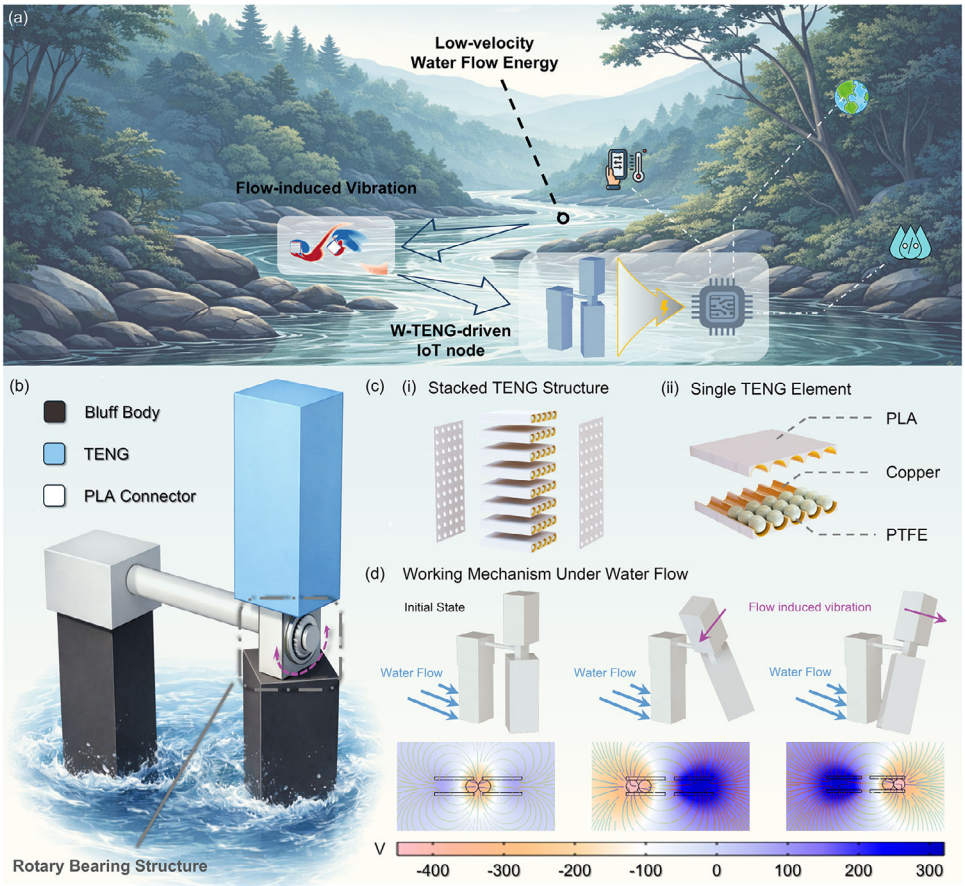


FIGURE 1 | Conceptual design, structural architecture, and working mechanism of the wake-induced vibration triboelectric nanogenerator (W-TENG). (a) Schematic illustration of the W-TENG deployed in a low-velocity river environment for self-powered ecological monitoring. (b) Overall structural configuration, consisting of an upstream stationary bluff body, a downstream oscillating bluff body, and an integrated TENG module. (c) (i) Exploded view of the stacked TENG module; (ii) Detailed structure of a single unit, showing arc-shaped tracks, copper electrodes, insulating layers, and PTFE rolling balls. (d) One complete operational cycle of the W-TENG, including wake-induced oscillation and the corresponding electric potential distribution simulated by COMSOL Multiphysics.

capable of transmitting data via Bluetooth to a mobile device for real-time monitoring. Overall, the proposed W-TENG provides a practical self-powered solution for river ecological monitoring sensors and offers an effective strategy for harvesting energy from low-velocity water flows.

2 | Results and Discussion

2.1 | Structural Design and Working Principle

Figure 1a depicts the application scenario of the proposed W-TENG, which is designed to harvest flow energy from low-velocity river environments. The working principle is based on wake-induced vibration: a stationary upstream bluff body generates vortices that excite the oscillatory motion of a downstream bluff body, thereby converting fluid kinetic energy into mechanical motion and ultimately into electricity. The harvested energy can be used to power electronic components such as sensors, LEDs, and timers, highlighting the potential of the W-TENG for river ecological monitoring applications. As shown in Figure 1b, the device can be divided into three modules: a stationary bluff body, a downstream oscillating bluff body, and a TENG module mounted atop the downstream body. Both bluff bodies are fully submerged in water, while the TENG module is positioned above the water surface, thereby minimizing water-induced charge dissipation and corrosion. The upstream and downstream bluff bodies are connected through a smooth shaft, while the downstream bluff body and the TENG module are rigidly linked by a bearing-supported PLA structure. Under the excitation of wake vortices generated by the upstream bluff body, the downstream bluff body undergoes periodic transverse vibration in the water flow, driving the swinging of the TENG module. In the absence of the upstream bluff body, only negligible oscillatory motion of the downstream bluff body was observed under the investigated flow conditions (Video S1), indicating that wake excitation is critical for inducing the oscillatory response of the system.

Figure 1c(i) presents an exploded view of the TENG module, which is composed of multiple individual unit modules. Baffles are installed on both sides to confine the movement of the balls, and adjacent units are electrically connected in series using copper foil. Figure 1c(ii) presents an exploded view of an individual unit. Each unit incorporates five arc-shaped tracks designed to increase the contact frequency between the balls and the copper electrodes, thereby enhancing power generation. Two

16163028, 2026, 71, Downloaded from https://advanced.onlinelibrary.wiley.com/doi/10.1002/adfm.77518 by Beihang University (Buaa), Wiley Online Library on [23/09/2026]. See the Terms and Conditions (https://onlinelibrary.wiley.com/terms-and-conditions) on Wiley Online Library for rules of use; OA articles are governed by the applicable Creative Commons License

copper electrodes are adhered to each track, separated by a PLA insulating layer. Each track contains a polytetrafluoroethylene (PTFE) ball that can freely roll from one side to the other following the periodic oscillation of the bluff body. By stacking multiple units, the design enables efficient space utilization while maintaining good replicability and allowing flexible addition or removal of individual units.

Figure 1d illustrates the three operational states within one working cycle. In the initial stationary state, water flowing past the upstream bluff body induces vortex shedding. The resulting wake vortices excite the downstream bluff body, generating a pressure difference across its surfaces that initiates oscillation about the bearing. Such bearing-centered swinging motion enables the PTFE balls to roll more easily inside the curved tracks, thereby promoting more effective triboelectric contact with the copper electrodes. As the downstream bluff body reaches one extreme swing angle, gravity acts to restore it toward the equilibrium position, while its inertia and the continuously generated wake from the upstream bluff body drive it toward the opposite extreme angle. This combined action results in sustained periodic oscillation, thereby completing a full vibration cycle. PTFE exhibits strong electronegativity. When PTFE comes into frictional contact with a material of different electronegativity, such as copper, charge transfer occurs, resulting in PTFE acquiring a negative charge and copper acquiring a positive charge, respectively. Consequently, as the TENG undergoes periodic swinging with the downstream bluff body, an alternating current is produced in the circuit. Based on the principles of electrostatic induction and charge conservation, simulation analysis of the potential difference distribution within the TENG module was conducted using COMSOL Multiphysics software. A three-dimensional model was constructed according to the actual structural parameters, and the dielectric and conductive properties of PTFE and Cu were defined to simulate the charge distribution of the PTFE ball at different swing positions. The results are in complete agreement with the theoretically analyzed patterns of charge transfer and current generation. These simulation results, from the perspective of electric field evolution, confirm the feasibility of the W-TENG's working mechanism and provide a theoretical basis for device structure optimization and performance enhancement.

2.2 | Bluff Body Selection

Since the output of the W-TENG module depends on the displacement and frequency of the downstream oscillating bluff body, and different bluff bodies exhibit distinct hydrodynamic responses which directly affect the overall output performance of the device, six bluff body combinations, as shown in Figure S1, were selected for investigation to determine the optimal configuration. To ensure consistent wake interaction conditions, a fixed spacing ratio of $L/D = 4$ was adopted for all tandem configurations. When both the upstream stationary bluff body and the downstream oscillating bluff body are cylinders, the overall oscillation is relatively regular and exhibits good periodicity at a low flow velocity of 0.18 m s^{-1}. However, as the flow velocity increases, the displacement of the bluff body decreases, and the motion loses its periodicity, showing an almost negligible displacement response (Figure 2a). When the upstream stationary bluff body is a cylinder, and the downstream oscillating bluff body is a square prism, the displacement of the bluff body is relatively regular within the flow velocity range of 0.18–0.4 m s^{-1}. However, unstable intervals exist, and the overall displacement is relatively small (Figure 2b). With a cylinder as the upstream stationary bluff body and a square prism at a 45° angle of attack as the downstream oscillating body, the bluff body exhibits larger displacement and good periodicity across the same velocity range (Figure 2c).

In the configuration with an upstream square prism and a downstream cylinder (Figure 2d), large and periodic displacements are observed at 0.18 and 0.26 m s^{-1}, whereas further increasing the flow velocity to 0.34 and 0.4 m s^{-1} leads to reduced displacement and loss of periodicity, with an almost negligible response at 0.4 m s^{-1}. Figure 2e demonstrates that when both the upstream and downstream bluff bodies are square prisms, there is almost no displacement response across the tested velocity range, and the system remains in a state of chaotic oscillation. In contrast, for the configuration consisting of an upstream square prism and a downstream square prism with a 45° angle of attack, the system maintains large displacement amplitudes and stable oscillation frequencies throughout the entire velocity range (Figure 2f). For clarity, the key response characteristics of all tested bluff body configurations are summarized in Table S1.

In summary, configurations with the downstream oscillating bluff body being a square prism at a 45° angle of attack consistently yield larger displacement responses, making it the optimal choice. Notably, while the combination with an upstream cylinder and a downstream square prism (45° angle of attack) shows unstable displacement at 0.34 and 0.4 m s^{-1}, the pairing of an upstream square prism with a downstream square prism (45° angle of attack) maintains stable periodic displacement even at these higher velocities. Therefore, the optimal bluff body combination for the W-TENG is determined to be: an upstream stationary square prism paired with a downstream oscillating square prism at a 45° angle of attack. All subsequent parameter optimization and performance testing are conducted based on this configuration. The superior performance of the 45° square prism originates from enhanced wake asymmetry and an increased transverse pressure gradient, which together promote stronger flow-induced excitation.

2.3 | Theoretical Model and Parameter Optimization of Wake-Induced Vibration

Effective excitation of the downstream bluff body through wake effects requires careful consideration of the flow characteristics around tandem bluff bodies. The vortex shedding behavior between the two bodies varies with different spacing distances, which consequently affects the motion pattern of the downstream bluff body and ultimately influences the voltage output of the TENG. As shown in Figure 3a, the spacing ratio L/D is an extremely critical parameter. Previous studies have shown that the vortex states between two tandem cylinders can be classified into three distinct regimes depending on the spacing ratio [50]. Under the condition where $L/D = 1$–2, the two cylinders behave hydrodynamically as a single enlarged body. In this regime, a single vortex street forms downstream of the combined structure, commonly referred to as the extended-body region. For the spacing ratio in the range of $L/D = 2$–5, only a pair of vortices

16163028, 2026, 71, Downloaded from https://advanced.onlinelibrary.wiley.com/doi/10.1002/adfm.77518 by Beihang University (Buaa), Wiley Online Library on [23/09/2026]. See the Terms and Conditions (https://onlinelibrary.wiley.com/terms-and-conditions) on Wiley Online Library for rules of use; OA articles are governed by the applicable Creative Commons License

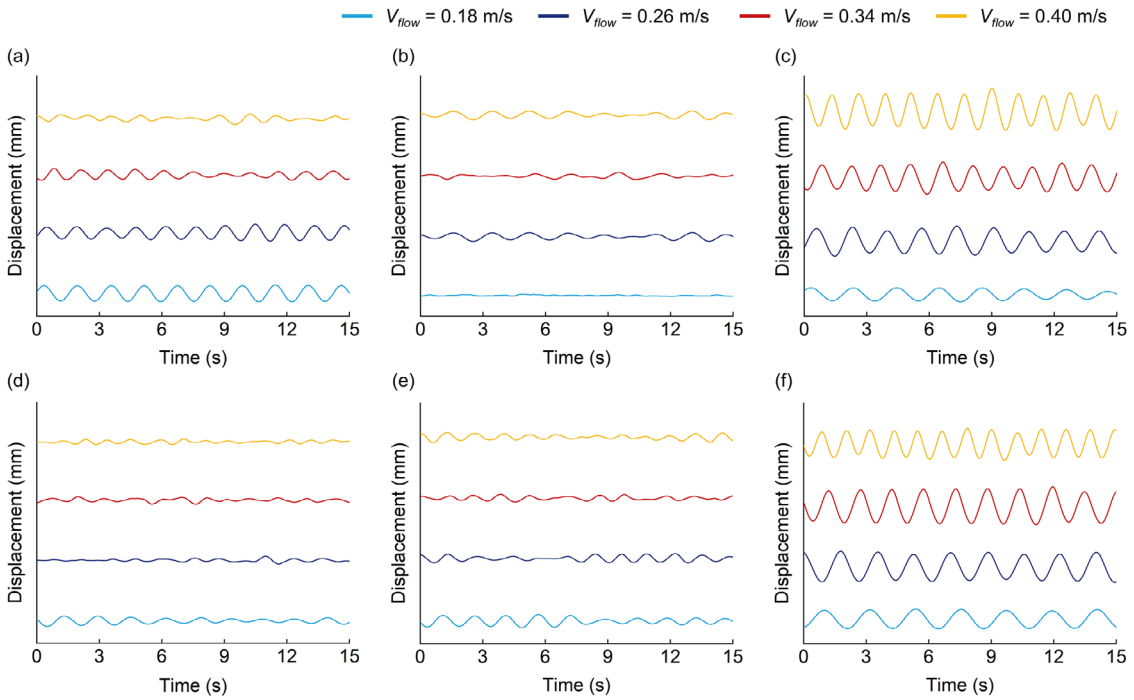


FIGURE 2 | Hydrodynamic displacement responses of the downstream bluff body under different tandem configurations. (a–f) Time-domain displacement curves at various flow velocities for six upstream-downstream bluff body combinations: (a) cylinder-cylinder; (b) cylinder-square prism; (c) cylinder-square prism (45° angle of attack); (d) square prism-cylinder; (e) square prism-square prism; (f) square prism-square prism (45° angle of attack).

exists within the gap between the cylinders. These vortices interact with the downstream cylinder and cause the shear layer to reattach to its surface, defining the reattachment region. When $L/D > 5$, fully developed vortex structures form within the gap. Separate, fully developed Kármán vortex streets are shed from both the upstream and downstream cylinders. This regime is termed the co-shedding region. With further increases in spacing, the hydrodynamic influence of the upstream stationary bluff body on the downstream oscillating bluff body gradually diminishes. When the spacing is sufficiently large, they can be considered as two independent systems in terms of hydrodynamics. Although these flow regimes were originally identified for tandem circular cylinders, the square prisms employed in this study are expected to exhibit qualitatively similar wake interaction behaviors due to the fundamental principles of flow continuity and fluid viscosity. Based on this consideration, four spacing ratios (L/D = 2, 3, 4, and 5) were selected as the primary variables for structural optimization of the W-TENG.

In this study, the downstream bluff body does not undergo pure translational motion but instead exhibits a fixed-axis rotational motion about the bearing, similar to that of a simple pendulum. Its dynamic behavior can therefore be described by the rotational form of Newton's second law: the product of the system's rotational inertia and angular acceleration is equal to the resultant external torque acting on the system. The modified control equation is:

$$I\ddot{\theta} + C_r\dot{\theta} + K_r\theta = M(t) \tag{1}$$

where I is the total rotational inertia of the downstream bluff body (including the top TENG module) relative to the rotation axis O. C_r is the rotational damping coefficient of the system, which includes bearing friction damping and fluid damping. K_r is the equivalent torsional stiffness of the system, provided by the restoring moment generated by gravity. θ is the angular displacement of the bluff body relative to the equilibrium position. $M(t)$ is the periodic fluid torque exerted by the upstream wake on the downstream bluff body.

The total rotational inertia of the system is calculated using the parallel axis theorem, considering the contributions of both the downstream bluff body and the TENG module:

$$I = I_1 + I_2 \tag{2}$$

Here, I_1 and I_2 represent the mass moments of inertia of the bluff body and the TENG module about the bearing axis O, respectively.

Experimental measurements indicate that at the maximum operating flow rate of 0.4 m s^{-1} in this device, the maximum oscillation angle of the downstream bluff body is ±26° (i.e., 0.454 rad). At this time, the relative error of the small-angle approximation $\sin\theta \approx \theta$ is:

$$\delta = \left|\frac{\theta - \sin\theta}{\sin\theta}\right| \times 100\% \approx 3.65\% \tag{3}$$

This error is lower than the 5% threshold commonly adopted in engineering analyses. Therefore, the small-angle approximation is considered reasonable within the operating range investigated in this work. Under the small-angle approximation, the lateral displacement y of the centroid of a bluff body and the angular

16163028, 2026, 71, Downloaded from https://advanced.onlinelibrary.wiley.com/doi/10.1002/adfm.77518 by Beihang University (Buaa), Wiley Online Library on [23/09/2026]. See the Terms and Conditions (https://onlinelibrary.wiley.com/terms-and-conditions) on Wiley Online Library for rules of use; OA articles are governed by the applicable Creative Commons License

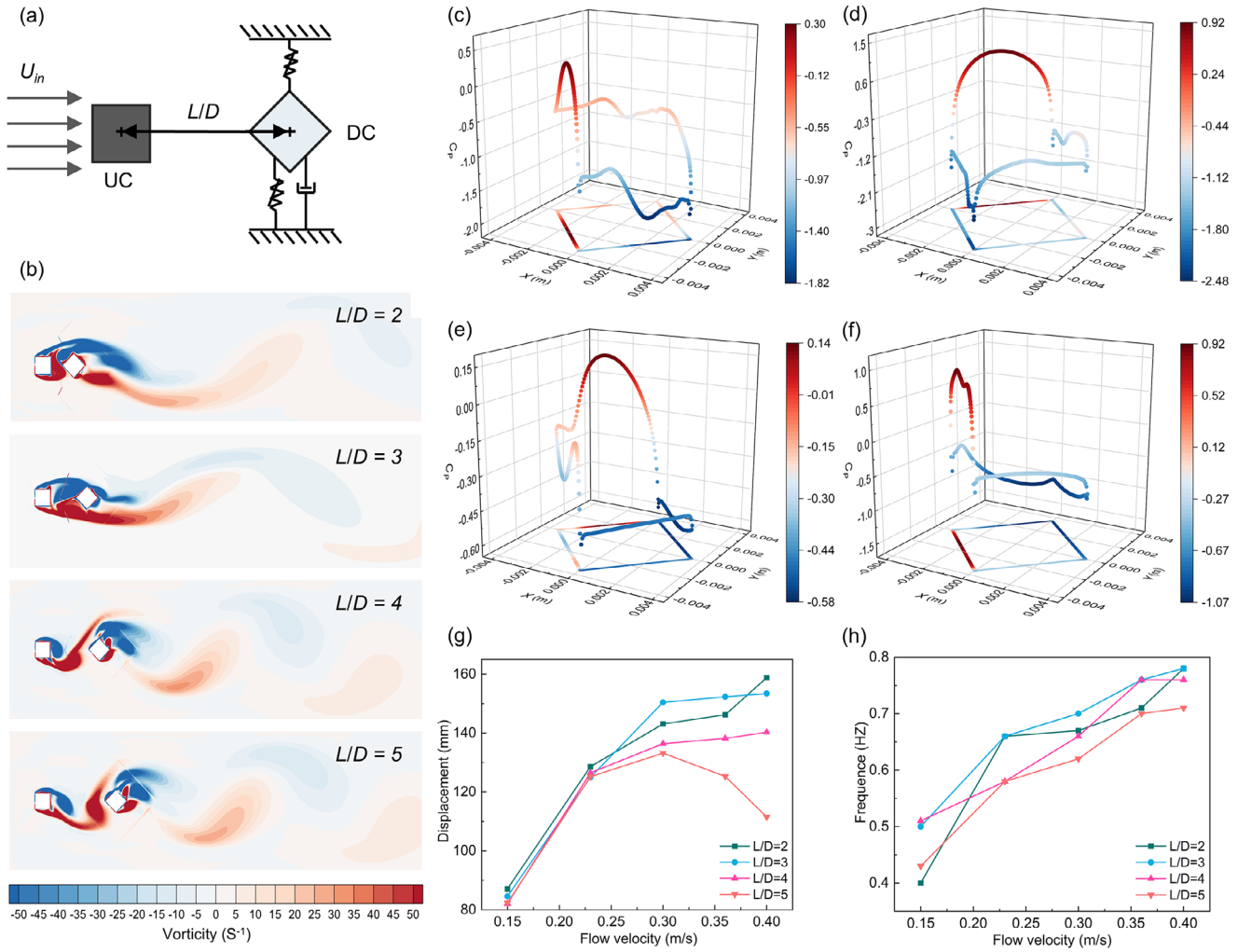


FIGURE 3 | Theoretical modeling and wake-excitation optimization of the W-TENG. (a) Single-degree-of-freedom dynamic model of the downstream oscillating bluff body. (b) CFD-derived velocity contour distributions for different spacing ratios (L/D). (c–f) Surface pressure coefficient (C_p) distributions on the downstream bluff body at $L/D = 2$, 3, 4, and 5, respectively. (g) Maximum oscillation amplitude as a function of flow velocity under different spacing ratios. (h) Oscillation frequency dependence on flow velocity for varying L/D values.

displacement θ satisfy:

$$y = d_1 \sin\theta \approx d_1\theta \tag{4}$$

Taking the first and second derivatives with respect to time t, the relationships between linear velocity and linear acceleration and angular velocity and angular acceleration are obtained:

$$\dot{y} \approx d_1\dot{\theta}, y \approx d_1\theta \tag{5}$$

Substituting Equation (5) into Equation (1) gives:

$$\frac{I}{d_1^2}y + \frac{Cr}{d_1^2}\dot{y} + \frac{K_r}{d_1^2}y = \frac{M(t)}{d_1} \tag{6}$$

In the formula $\frac{I}{d_1^2}$, $\frac{Cr}{d_1^2}$, $\frac{K_r}{d_1^2}$ and $\frac{M(t)}{d_1}$ represent the equivalent translational mass(m), equivalent translational damping(c), equivalent translational stiffness(k), and equivalent fluid force, respectively. Under the small-angle approximation, the rotational pendulum model can be reduced to the original translational form within the oscillation range of ±26°, yielding [51]:

$$my + c\dot{y} + ky = F \tag{7}$$

where m is the mass of the bluff body, c is the damping coefficient, k is the spring stiffness, and F is the force acting on the bluff body. The motion of the bluff body is sinusoidal, and its dimensionless displacement can be expressed as:

$$y(t) = y_0 \sin(\omega t) \tag{8}$$

where y_0 is the vibration amplitude, and ω is the angular frequency. Differentiating Equation (8) with respect to time yields the velocity in the displacement direction:

$$\dot{y}(t) = y_0\omega\cos(\omega t) \tag{9}$$

The energy harvested by the bluff body over an entire motion cycle can be expressed as:

$$E = \int_0^T F\dot{y}(t)\,dt \tag{10}$$

16163028, 2026, 71, Downloaded from https://advanced.onlinelibrary.wiley.com/doi/10.1002/adfm.77518 by Beihang University (Buaa), Wiley Online Library on [23/09/2026]. See the Terms and Conditions (https://onlinelibrary.wiley.com/terms-and-conditions) on Wiley Online Library for rules of use; OA articles are governed by the applicable Creative Commons License

Employing the dimensionless amplitude, mass ratio, damping ratio, and reduced velocity, the expression can be further simplified to:

$$E \propto f_{versus} y_0 \tag{11}$$

Assuming the dimensions of the bluff body remain constant, E is primarily influenced by the vortex shedding frequency and the oscillation amplitude.

To investigate the influence of the spacing ratio between two bluff bodies on the wake excitation effect and its mode, we selected four spacing ratios (L/D) of 2, 3, 4, and 5, and performed CFD simulations at a Reynolds number of 10500 (corresponding to an actual flow velocity of 0.3 m s^{-1}). In this study, the bluff body was simplified in the CFD simulation as a fixed model to investigate the influence of different L/D ratios on the vortex shedding characteristics. Since the purpose of the numerical analysis is to clarify the dominant flow mechanism rather than to predict the structural vibration response, this simplification is considered appropriate for explaining the performance differences observed in the experiments. Figure S2 shows the structural mesh drawn in ICEM. The overset mesh method was utilized, with the upstream and downstream bluff bodies designated as Overset regions, respectively. Table S2 presents the mesh- and time-step-independence analyses. Cases 1–3 were used to examine mesh convergence. The difference in root-mean-square value of the lift coefficient ($C_{L,\,rms}$) between Cases 2 and 3 is only 1.8%, indicating satisfactory mesh convergence. Cases 2, 4, and 5 were used to evaluate time-step independence, and the corresponding variations in $C_{L,\,rms}$ are within 5%. Therefore, Case 2 was selected for all subsequent simulations. The simulation parameters were determined based on the experimental conditions. Figure 3b shows the vorticity contours of the flow field for different spacing ratios. To further visualize the evolution of the wake flow, streamline distributions for different spacing ratios are provided in Figure S3. Based on the flow structure characteristics, the regimes can be categorized into three typical regions: At L/D = 2, the separated shear layers from the upstream bluff body extend beyond the downstream bluff body, corresponding to the extended-body regime. At L/D = 3, the separated shear layers reattach to the downstream bluff body, corresponding to the reattachment regime. At L/D = 4 and 5, the shear layers alternately roll up into vortices, generating vortex streets within the gap and in the wake of the tandem bluff bodies, corresponding to the co-shedding regime.

To quantitatively analyze the excitation intensity on the downstream bluff body under different conditions, the surface pressure coefficient (C_p) was introduced as an evaluation metric. The C_p is a core dimensionless parameter in fluid mechanics that characterizes the relative strength of pressure exerted by the fluid on a solid surface. Its primary value lies in eliminating the influence of operational parameters such as fluid density and inflow velocity, directly revealing the relative patterns of pressure distribution, the degree of pressure recovery in the wake, and the strength of vortex shedding. It is a key indicator for assessing the magnitude of vortex-induced forces and, consequently, the potential for energy harvesting. Figure 3c–f shows the surface pressure coefficient distributions on the downstream bluff body for spacing ratios of L/D = 2–5. The pressure difference between the two lateral sides of the bluff body in the cross-flow direction is crucial for its motion. It can be observed that at L/D = 3, the maximum pressure coefficient difference across the bluff body is 2.79, which is significantly higher than those of the other configurations. A larger pressure difference across the two lateral surfaces of the downstream bluff body corresponds to a stronger transverse fluid force, thereby providing more effective wake-induced excitation. Consequently, the L/D = 3 configuration is expected to provide stronger wake-induced excitation. Figure S4 shows the lift coefficients of the bluff body under different spacing ratios. The lift coefficient reaches a peak value of 3.38 at L/D = 3 and gradually decreases with increasing spacing ratio, consistent with the trend observed for ΔC_p. This can be explained as follows: in the extended body regime, the shear layer bypasses the bluff body, resulting in smaller hydrodynamic forces; in the reattachment regime, the wake excitation increases due to the direct influence of the newly formed vortices; as the gap ratio increases further, the influence of the wake vortices diminishes. Notably, the wake-induced pressure difference governs the excitation force acting on the downstream bluff body, thereby influencing the conversion of flow energy into mechanical energy. To further examine the influence of flow velocity, additional simulations were conducted for the L/D = 3 configuration at Reynolds numbers of 5250 and 14000 (corresponding to flow velocities of 0.15 and 0.4 m s^{-1}, respectively). As shown in Figure S5, the pressure coefficient difference (ΔC_p) increases with increasing flow velocity while maintaining a similar pressure-distribution pattern.

To validate the simulation results, the bluff body displacement and frequency under different spacing ratios were measured experimentally, as shown in Figure 3g,h. It can be observed that for L/D = 2, 3, and 4, the maximum displacement of the bluff body increases with the flow velocity. For L/D = 5, the oscillation amplitude decreases when the flow velocity exceeds 0.3 m s^{-1}. This behavior may be attributed to the reduced effectiveness of wake-induced excitation under the enlarged spacing condition. As the downstream bluff body moves farther from the strong wake-interference region, the periodic excitation from the upstream wake becomes less effective, leading to a reduced vibration response. Regarding frequency characteristics, the oscillation frequency of the bluff body increases with the inflow velocity under all conditions. Particularly under the condition of L/D = 3, the frequency is higher than that of the other parameters. Equation (11) indicates that the harvested energy is closely associated with the oscillation amplitude and characteristic frequency of the downstream bluff body. The CFD results show that the L/D = 3 configuration generates the strongest wake-induced excitation, and the experimentally measured displacement and frequency further support this trend. Therefore, L/D = 3 is determined as the optimal design parameter for this structure.

2.4 | Performance Testing and Applications

To evaluate the power generation performance of the W-TENG, the experimental setup shown in Figure 4a was constructed under controlled water flow conditions. Stable flow velocities from 0 to 0.4 m s^{-1} were generated using a water pump controlled by a variable frequency drive. The W-TENG was secured to an aluminum profile frame at the center of the water channel, placing it within

16163028, 2026, 71, Downloaded from https://advanced.onlinelibrary.wiley.com/doi/10.1002/adfm.77518 by Beihang University (Buaa), Wiley Online Library on [23/09/2026]. See the Terms and Conditions (https://onlinelibrary.wiley.com/terms-and-conditions) on Wiley Online Library for rules of use; OA articles are governed by the applicable Creative Commons License

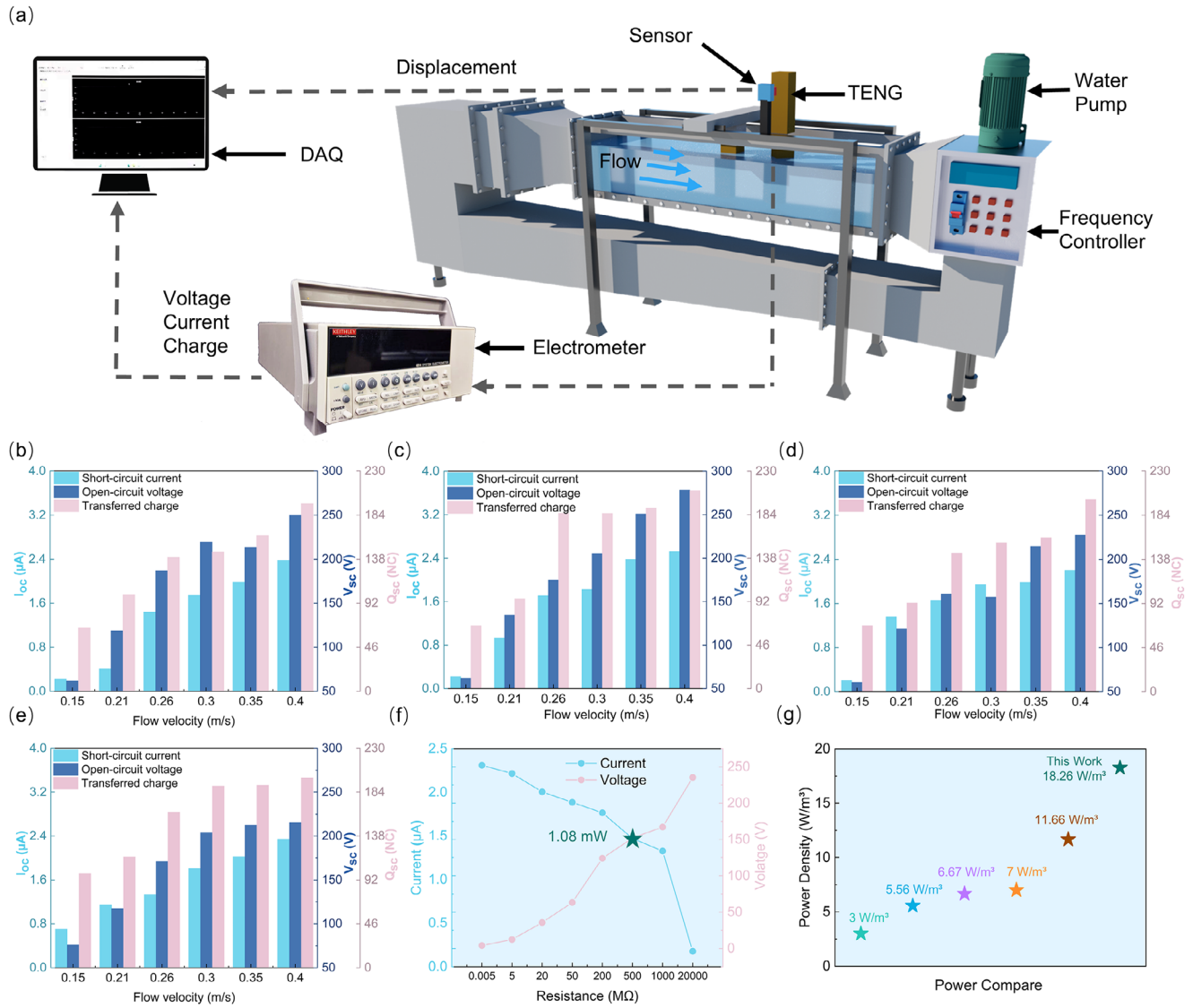


FIGURE 4 | Electrical output performance and load matching characteristics of the W-TENG. (a) Experimental setup for performance evaluation under controlled flow velocities. (b–e) Output voltage, current, and transferred charge at different spacing ratios ($L/D = 2, 3, 4, 5$). (f) Load resistance dependence of output power at the optimal spacing ratio ($L/D = 3$). (g) Comparison of volumetric power density with previously reported low-velocity water-flow TENGs [30, 31, 40, 52, 53].

the core region of the flow field. The displacement of the W-TENG was captured by a sensor, recorded through a data acquisition (DAQ) card, and visualized in LabVIEW. Concurrently, the electrical output parameters, including the short-circuit current, open-circuit voltage, and transferred charge, were measured and recorded using a grounded electrometer to minimize external electrostatic interference. Electrical output performance was evaluated at four spacing ratios ($L/D = 2, 3, 4$, and 5), as shown in Figure 4b–e. As the imposed flow velocity increased from 0.15 to 0.4 m s^{-1}, both the output current and transferred charge increased accordingly. Among the tested configurations, $L/D = 3$ showed the most consistent increase in output voltage with flow velocity and exhibited superior electrical performance. In contrast, the voltage responses at $L/D = 2$ and 4 were non-monotonic. This behavior is associated with variations in the wake interactions between the upstream and downstream bluff bodies, leading to distinct vibration responses and electrical outputs. With $L/D = 3$, the W-TENG exhibited stable periodic vibration and continuous electrical output at a flow velocity of 0.15 m s^{-1}, demonstrating its operational capability under ultra-low flow conditions. At a flow velocity of 0.4 m s^{-1}, it achieved a peak output voltage of 278.55 V, a current of 2.52 μA, and a transferred charge of 209.7 nC. Based on the optimal structure with $L/D = 3$, the load matching analysis (Figure 4f) reveals an optimal load resistance of 500 MΩ, corresponding to a peak output power of 1.08 mW. As shown in Figure 4g, the peak volumetric power density of the designed W-TENG reaches 18.26 W m^{-3}. The power density was calculated according to:

$$P_{density} = \frac{I^2 R}{V} \tag{12}$$

where V represents the volume of the TENG unit directly involved in the mechanical-to-electrical energy conversion process. A comparison with representative low-velocity water flow

16163028, 2026, 71, Downloaded from https://advanced.onlinelibrary.wiley.com/doi/10.1002/adfm.77518 by Beihang University (Buaa), Wiley Online Library on [23/09/2026]. See the Terms and Conditions (https://onlinelibrary.wiley.com/terms-and-conditions) on Wiley Online Library for rules of use; OA articles are governed by the applicable Creative Commons License

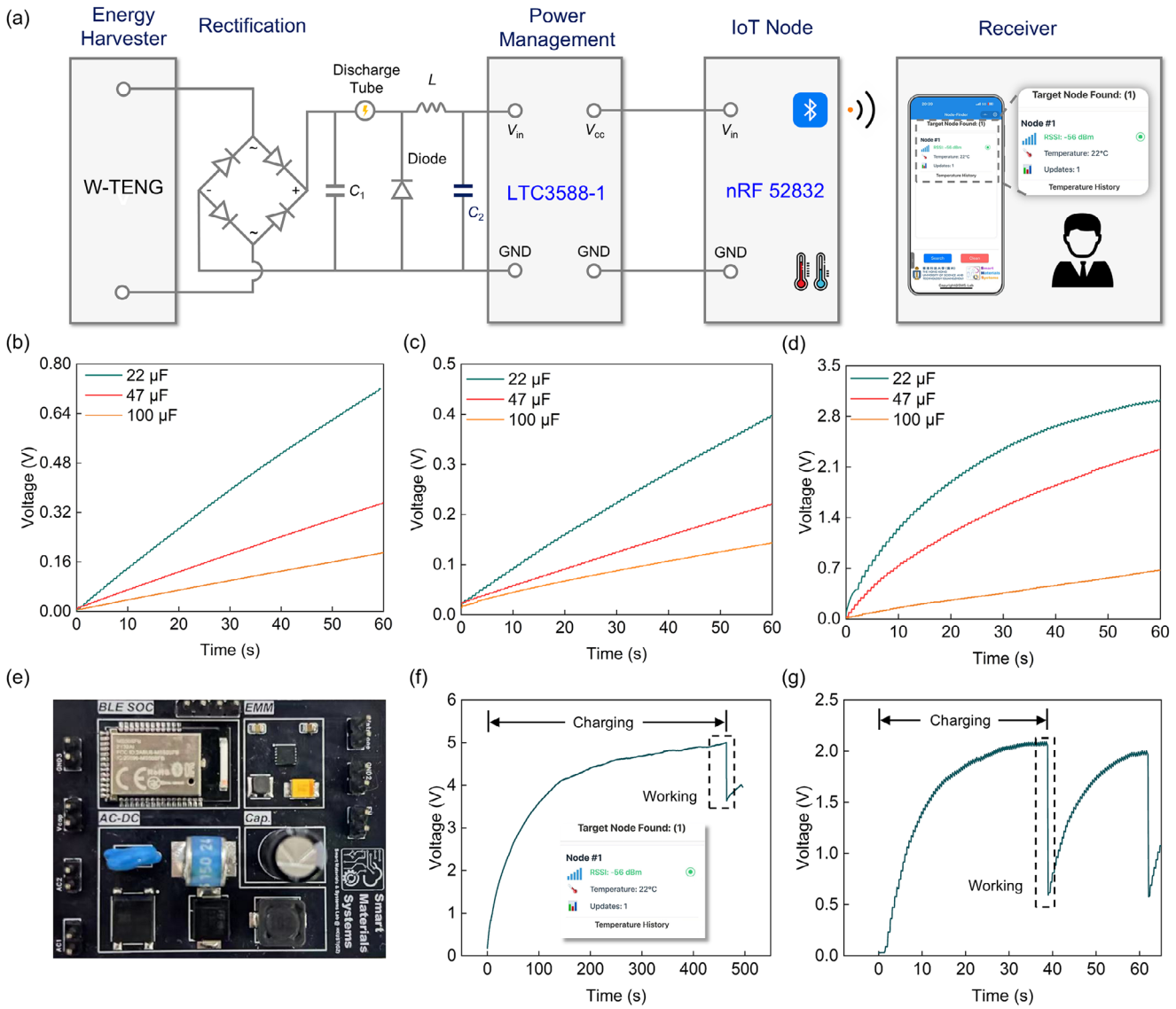


FIGURE 5 | Energy management strategy and practical application demonstrations of the W-TENG. (a) Schematic diagram of the integrated energy management circuit. (b) Capacitor charging profiles without power management. (c,d) Charging performance with different discharge tubes (90 and 150 V). (e) Physical diagram of the wireless temperature sensor system (f) Demonstration of the W-TENG powering a wireless temperature sensor. (g) Continuous operation of an electronic timer powered by the W-TENG.

energy harvesters is summarized in Table S3, demonstrating the effectiveness of the proposed wake-excitation strategy.

Through the aforementioned research, the optimal parameters for the W-TENG have been determined, and its in-water performance output has been tested. Figure 5a shows the energy management circuit schematic, where the entire system consists of three main parts. The first part is the rectification stage. The TENG generates an alternating current (AC) output through mechanical-to-electrical energy conversion. The bridge rectifier converts the AC output into a direct current (DC) output. The second part is the energy management module, which consists of the energy-harvesting power management integrated circuit LTC3588-1, a storage capacitor C_1, a discharge tube, an inductor L, and an output capacitor C_2, forming a DC-DC energy conditioning circuit. This circuit stores and transfers the rectified output, while the LTC3588-1 power management chip regulates the stored energy for subsequent load operation. C_1 temporarily stores the harvested energy. The discharge tube serves as a voltage-triggered switching device, remaining in a high-impedance state prior to breakdown and rapidly becoming conductive once the voltage across it reaches the breakdown threshold. Assisted by the switching devices and inductor L, the harvested energy is efficiently transferred to and stored in C_2. Once the voltage supplied to the LTC3588-1 exceeds its undervoltage lockout (UVLO) threshold, the chip provides a regulated DC output to the load, preventing premature power delivery. The final part is the application side. The load is a System on Chip (SoC) that integrates a Bluetooth Low Energy (BLE) communication module and a temperature sensor. It is powered by the output of the power management unit. During operation, the sensor acquires environmental parameter. After processing by the SoC, the sensing data is wirelessly

16163028, 2026, 71, Downloaded from https://advanced.onlinelibrary.wiley.com/doi/10.1002/adfm.77518 by Beihang University (Buaa), Wiley Online Library on [23/09/2026]. See the Terms and Conditions (https://onlinelibrary.wiley.com/terms-and-conditions) on Wiley Online Library for rules of use; OA articles are governed by the applicable Creative Commons License

transmitted to a mobile device via the BLE module, thereby realizing self-powered wireless monitoring.

Figure 5b shows the capacitor charging speed of the W-TENG without an energy management circuit. Under a flow velocity of 0.4 m s^{-1} and a charging duration of 60 s, the W-TENG charged a 22 μF capacitor from 0 to 0.71 V, a 47 μF capacitor to 0.38 V, and a 100 μF capacitor to 0.18 V. Figure 5c,d present the charging speeds of the W-TENG with an energy management circuit incorporating discharge tubes of 90 V and 150 V, respectively, for different capacitors. The results indicate that the 150 V discharge tube yields the best performance, which can be attributed to its ability to allow more electrical energy to accumulate before each discharge event. Figure S6 shows photographs of the circuit boards containing the 90 and 150 V discharge tubes. Under identical operating conditions, the 22, 47, and 100 μF capacitors are charged to 3.03 , 2.33, and 0.67 V, respectively, corresponding to charging rate enhancements of 4.27, 6.13, and 3.72. The improved charging performance mainly arises from the breakdown-mediated release of accumulated energy through the discharge tube, which enables harvested energy to be delivered more effectively to C_2.

Figure 5e shows the physical image of the wireless temperature sensor. As shown in Figure 5f, under a flow velocity of 0.4 m s^{-1}, the W-TENG charged a 47 μF capacitor to 5 V. The stored energy subsequently enabled wireless temperature sensing and real-time data display on a mobile phone. Once the stored energy was depleted below the operating threshold, the system returned to the charging state. In addition, the W-TENG is capable of continuously driving an electronic timer, demonstrating stable and uninterrupted operation (Figure 5g). A detailed demonstration of the capacitor charging process and the operation of the temperature sensor and electronic timer is provided in Videos S2 and S3. This demonstrates the capability of the W-TENG to function as a fully self-sustained sensing node, enabling a closed-loop energy-data system without reliance on external power sources. The reliability of the W-TENG was further evaluated through seven-day electrical output monitoring and a 2000 s continuous cycling test (Figures S7 and S8). The results show stable output characteristics without noticeable performance attenuation, demonstrating the reliable operation of the device under prolonged and continuous working conditions. To further demonstrate its field adaptability, the operation of the W-TENG in a natural stream environment is shown in Video S4.

3 | Conclusions

This work addresses key challenges in harvesting energy from shallow and low-velocity water environments, including low conversion efficiency, high cut-in flow velocities, and poor structural adaptability of existing systems. We propose a **wake-induced vibration triboelectric nanogenerator (W-TENG)** as an effective and scalable solution for energy harvesting in such conditions. An optimal bluff body configuration was identified, consisting of an upstream square prism and a downstream square prism oriented at a 45° angle of attack. Combined CFD simulations and experimental analyses revealed that at a spacing ratio of $\boldsymbol{L/D = 3}$, the downstream bluff body exhibited the highest-pressure coefficient difference ($\Delta C_p = 2.79$) and lift coefficient ($C_L = 3.38$), corresponding to the strongest wake-induced excitation and optimal energy transfer conditions. Performance evaluations demonstrated the W-TENG's excellent compatibility with low-velocity flows. At a flow speed of **0.4 m $\mathbf{s^{-1}}$**, it achieved a peak volumetric power density of **18.26 W $\mathbf{m^{-3}}$**, outperforming previously reported low-velocity TENGs. Furthermore, by integrating an optimized energy management circuit, the capacitor charging rate was significantly enhanced. Application demonstrations showed that the W-TENG could reliably power both an electronic timer and a wireless temperature sensor, enabling autonomous operation and real-time data transmission without external power. These results validate the system's robustness and practical utility for **self-powered, low-power sensor nodes** in riverine ecological monitoring. In summary, this study establishes a rational and efficient design framework that leverages wake-induced vibration to activate TENGs, enabling the effective transduction of low-speed hydrodynamic energy into electricity. The proposed design principle can be readily extended to other flow-induced energy harvesting systems, offering a general framework for exploiting low-grade fluid energy. The proposed W-TENG offers a compelling pathway toward sustainable, self-powered sensing platforms for smart water environments.

4 | Experimental Section

4.1 | Fabrication of the W-TENG

The upstream stationary bluff body, the downstream oscillating bluff body, the connectors, as well as the individual units and the housing of the TENG module were all fabricated using 3D printing. The printing equipment was a Bambu Lab X1 Carbon, and the material was PLA. The dimensions of the square prism bluff bodies are 35 mm × 35 mm × 100 mm. The upstream bluff body is fixed beneath an aluminum profile frame via connectors. The TENG module is composed of 11 units, each measuring 32 mm × 28 mm × 6 mm. Within each unit, there are five arc-shaped tracks with a diameter of 5.8 mm and an inter-track spacing of 0.6 mm. A 60 μm thick copper foil, serving as an electrode, is adhered to each track. The spacing between adjacent copper foils is 3 mm. Each track contains three PTFE balls with a diameter of 5 mm, which can roll freely back and forth within the track. The TENG module is mounted atop the downstream oscillating bluff body via connectors. A stainless-steel bearing with an inner diameter of 8 mm is installed at the center of the connector assembly. The upstream and downstream bluff bodies are linked by a stainless-steel rod passing through this bearing, allowing for free adjustment of the spacing between them.

4.2 | Electrical Measurements

The open-circuit voltage, short-circuit current, and transferred charge of the TENG were measured using a programmable electrometer (Model 6514, Keithley). For displacement measurements, a high-precision infrared displacement sensor was employed. Data visualization and processing were conducted on a PC using LabVIEW software.

16163028, 2026, 71, Downloaded from https://advanced.onlinelibrary.wiley.com/doi/10.1002/adfm.77518 by Beihang University (Buaa), Wiley Online Library on [23/09/2026]. See the Terms and Conditions (https://onlinelibrary.wiley.com/terms-and-conditions) on Wiley Online Library for rules of use; OA articles are governed by the applicable Creative Commons License

Acknowledgements

This study was partially supported by the Outstanding Youth Science Fund Rolling Support Project of Henan Province under Grant number 252300421239 and the National Natural Science Foundation of China under Grant numbers (52277227, 52125205, 52532005 and 52250398), National Key Research and Development (R&D) Program from Ministry of Science and Technology of China (2024YFB3814100), Natural Science Foundation of Beijing Municipality (2222088 and L223006), and the Fundamental Research Funds for the Central Universities. The authors also thank Xuzhou B&C Chemical Co. Ltd for providing the photoresist (HTA116, HTA112, B&C Chemicals) used in our work.

Conflicts of Interest

The authors declare no conflicts of interest.

Data Availability Statement

The data that support the findings of this study are available from the corresponding author upon reasonable request.

References

1. S. Zhang, Z. Jing, X. Wang, et al., "Enhancing Low-Velocity Water Flow Energy Harvesting of Triboelectric–Electromagnetic Generator via Biomimetic-Fin Strategy and Swing-Rotation Mechanism," *ACS Energy Letters* 7 (2022): 4282–4289.

2. T. Li, C. Li, K. Wang, et al., "A Triboelectric–Electromagnetic Hybrid Generator for Harvesting River Energy and Wind Energy for River Ecosystem Monitoring," *ACS Applied Materials & Interfaces* 16 (2024): 33347–33359.

3. X. L. Kang, P. B. Li, D. Yurchenko, S. G. Dai, and J. L. Wang, "Fundamental Theory and Cutting-Edge Applications of TENGs," *Mater Futures* 4 (2025): 042101.

4. D. W. Jiang, M. Y. Lian, M. J. Xu, et al., "Advances in Triboelectric Nanogenerator Technology-Applications in Self-Powered Sensors, Internet of Things, Biomedicine, and Blue Energy," *Advanced Composites and Hybrid Materials* 6 (2023): 57.

5. X. L. Cao, Y. Xiong, J. Sun, X. Y. Xie, Q. J. Sun, and Z. L. Wang, "Multidiscipline Applications of Triboelectric Nanogenerators for the Intelligent Era of Internet of Things," *Nano-Micro Letters* 15 (2023): 41.

6. D. Liu, J. Luo, L. Huang, et al., "Triboelectric Nanogenerators as a Practical Approach for Wind Energy Harvesting: Mechanisms, Designs, and Applications," *Nano Energy* 136 (2025): 110767.

7. X. Liang, S. Liu, Z. Ren, T. Jiang, and Z. L. Wang, "Self-Powered Intelligent Buoy Based on Triboelectric Nanogenerator for Water Level Alarming," *Advanced Functional Materials* 32 (2022): 2205313.

8. H. Zhou, X. Wei, B. Wang, E. Zhang, Z. Wu, and Z. L. Wang, "A Multi-Layer Stacked Triboelectric Nanogenerator Based on a Rotation-to-Translation Mechanism for Fluid Energy Harvesting and Environmental Protection," *Advanced Functional Materials* 33 (2023): 2210920.

9. A. Ahmed, I. Hassan, M. F. El-Kady, et al., "Integrated Triboelectric Nanogenerators in the Era of the Internet of Things," *Advancement of Science* 6 (2019): 1802230.

10. J. X. Zhu, M. L. Zhu, Q. F. Shi, et al., "Progress in TENG Technology-A Journey From Energy Harvesting to Nanoenergy and Nanosystem," *EcoMat* 2 (2020): 12058.

11. S. Roy, B. Dudem, M. D. Hussain, et al., "Ultra-Sensitive Nanofiber-Based Triboelectric Nanogenerator for Energy Harvesting and Self-Powered Sensing," *Advanced Materials* 38 (2026): 21626.

12. W. G. Kim, D. W. Kim, I. W. Tcho, J. K. Kim, M. S. Kim, and Y. K. Choi, "Triboelectric Nanogenerator: Structure, Mechanism, and Applications," *ACS Nano* 15 (2021): 258–287.

13. Y. Zhang, H. Wang, Y. W. Wang, et al., "Underwater Blade-free Triboelectric Nanogenerator for Harvesting Current Energy in Low-speed Current," *Nano Energy* 131 (2024): 110290.

14. Y. Zhao, W. Gao, K. Dai, et al., "Bioinspired Multifunctional Photonic-electronic Smart Skin for Ultrasensitive Health Monitoring, for Visual and Self-powered Sensing," *Advanced Materials* 33 (2021): 2102332.

15. S. B. Chen, S. Li, G. H. Wang, and K. P. Yu, "Finite-horizon Energy Allocation Scheme in Energy Harvesting-based Linear Wireless Sensor Network," *Future Generation Computer Systems* 162 (2025): 107493.

16. Y. Peng, J. Lu, X. Wang, et al., "Self-powered High-performance Flexible GaN/ZnO Heterostructure UV Photodetectors With Piezo-phototronic Effect Enhanced Photoresponse," *Nano Energy* 94 (2022): 106945.

17. I. Escuder-Bueno, J. T. Castillo-Rodríguez, S. Zechner, C. Jöbstl, S. Perales-Momparler, and G. Petaccia, "A Quantitative Flood Risk Analysis Methodology for Urban Areas With Integration of Social Research Data," *Nat Hazards Earth Syst Sci* 12 (2012): 2843–2863.

18. Y. L. Zi, H. Y. Guo, Z. Wen, M. H. Yeh, C. G. Hu, and Z. L. Wang, "Harvesting Low-Frequency (<5 Hz) Irregular Mechanical Energy: A Possible Killer Application of Triboelectric Nanogenerator," *ACS Nano* 10 (2016): 4797–4805.

19. J. Q. Zhao, G. W. Zhen, G. X. Liu, et al., "Remarkable Merits of Triboelectric Nanogenerator Than Electromagnetic Generator for Harvesting Small-amplitude Mechanical Energy," *Nano Energy* 61 (2019): 111–118.

20. C. Zhang, W. Tang, C. Han, F. Fan, and Z. L. Wang, "Theoretical Comparison, Equivalent Transformation, and Conjunction Operations of Electromagnetic Induction Generator and Triboelectric Nanogenerator for Harvesting Mechanical," *Energy* 26 (2014): 3580–3591.

21. H. Yu, D. Sun, W. Dong, et al., "All-In-One Flexible Thermoelectric Yarns for Integrated Energy Harvesting," *Advanced Functional Materials* 36 (2026): 25233.

22. J. Meng, Q. Li, J. Huang, C. Pan, and Z. Li, "Self-powered Photodetector for Ultralow Power Density UV Sensing," *Nano Today* 43 (2022): 101399, https://doi.org/10.1016/j.nantod.2022.101399.

23. Z. L. Wang, "Triboelectric Nanogenerator (TENG)-Sparking an Energy and Sensor Revolution," *Advanced Energy Materials* 10 (2020): 2000137.

24. Z. L. Wang, T. Jiang, and L. Xu, "Toward the Blue Energy Dream by Triboelectric Nanogenerator Networks," *Nano Energy* 39 (2017): 9–23, https://doi.org/10.1016/j.nanoen.2017.06.035.

25. F. R. Fan, Z. Q. Tian, and Z. L. Wang, "Flexible triboelectric generator," *Nano Energy* 1 (2012): 328–334, https://doi.org/10.1016/j.nanoen.2012.01.004.

26. F. R. Fan, W. Tang, and Z. L. Wang, "Flexible Nanogenerators for Energy Harvesting and Self-Powered Electronics," *Advanced Materials* 28 (2016): 4283–4305.

27. H. C. Luo, X. Y. Ni, Y. X. Cui, et al., "High Stability Rotary Solid-liquid Triboelectric Nanogenerator for Ionic Liquid Detection," *Nano Energy* 138 (2025): 110870.

28. Z. Deng, L. Xu, H. Qin, et al., "Rationally Structured Triboelectric Nanogenerator Arrays for Harvesting Water-Current Energy and Self-Powered Sensing," *Advanced Materials* 34 (2022): 2205064.

29. Y. Zheng, T. Liu, J. Wu, et al., "Energy Conversion Analysis of Multilayered Triboelectric Nanogenerators for Synergistic Rain and Solar Energy Harvesting," *Advanced Materials* 34 (2022): 2202238.

30. A. Jin, X. B. Gao, X. K. Hang, et al., "Double Helix Rotating TENGs Driven by Ultra-low Loading for Harvesting High-entropy Water Flow Energy," *Renewable Energy* 238 (2025): 121919.

31. Z. X. Jing, J. C. Zhang, J. L. Wang, M. K. Zhu, and X. X. Wang, "3D Fully-Enclosed Triboelectric Nanogenerator With Bionic Fish-Like Structure for Harvesting Hydrokinetic Energy," *Nano Research* 15 (2022): 5098–5104, https://doi.org/10.1007/s12274-022-4131-y.

16163028, 2026, 71, Downloaded from https://advanced.onlinelibrary.wiley.com/doi/10.1002/adfm.77518 by Beihang University (Buaa), Wiley Online Library on [23/09/2026]. See the Terms and Conditions (https://onlinelibrary.wiley.com/terms-and-conditions) on Wiley Online Library for rules of use; OA articles are governed by the applicable Creative Commons License

32. T. Y. Li, C. X. Li, K. K. Wang, et al., "Hierarchical Structure-based Biomimetic Triboelectric-electromagnetic Hybrid Generator for River Monitoring," *Chemical Engineering Journal* 509 (2025): 161035.

33. X. Huang, C. Y. Xing, Z. H. Zhou, et al., "Underwater High-performance Flag-shaped Triboelectric Nanogenerator for Harvesting Energy in Ultraslow Water Current," *Nano Energy* 135 (2025): 110664.

34. P. Han, Q. G. Huang, and G. Pan, "Optimal Energy Harvesting Efficiency From Vortex-induced Vibration of a Circular Cylinder," *Ocean Engineering* 282 (2023): 114869.

35. J. L. Wang, L. F. Geng, L. Ding, H. J. Zhu, and D. Yurchenko, "The State-of-the-Art Review on Energy Harvesting From Flow-induced Vibrations," *Applied Energy* 267 (2020): 114902.

36. X. Q. Ma and S. X. Zhou, "A Review of Flow-induced Vibration Energy Harvesters," *Energy Conversion and Management* 254 (2022): 115223, https://doi.org/10.1016/j.enconman.2022.115223.

37. J. L. Wang, P. B. Li, X. L. Kang, Z. J. Li, and S. G. Dai, "Soft-soft Contact TENG Using Nonlinear Coupling Galloping Phenomenon for Harvesting Wind Energy," *Nano Energy* 133 (2025): 110471.

38. C. T. Shen, X. L. Kang, R. Y. Zhang, and J. L. Wang, "The Influence of Vortex Shedding on the Flag Triboelectric Nanogenerators," *Nano Energy* 146 (2025): 111564.

39. L. H. Jiang, X. L. Liu, J. L. Lv, et al., "Fluid-based Triboelectric Nanogenerators: Unveiling the Prolific Landscape of Renewable Energy Harvesting and Beyond," *Energy & Environmental Science* 17 (2024): 3700–3738.

40. S. Zhang, Z. X. Jing, X. X. Wang, et al., "Soft-Bionic-fishtail Structured Triboelectric Nanogenerator Driven by Flow-induced Vibration for Low-velocity Water Flow Energy Harvesting," *Nano Research* 16 (2023): 466–472.

41. Y. Wang, X. Y. Liu, T. Y. Chen, et al., "An Underwater Flag-Like Triboelectric Nanogenerator for Harvesting Ocean Current Energy Under Extremely Low Velocity Condition," *Nano Energy* 90 (2021): 106503.

42. B. Y. Li, H. C. Li, Y. J. Zhong, et al., "Flow-induced Vibrations of a Square Cylinder at Different Angles of Attack: The Importance of the in-line Vibrations," *Physics of Fluids* 37 (2025): 023614.

43. C. Liu, B. Zhang, L. Dong, J. Zhong, J. Wang, and Y. Wang, "A Review of Energy Harvesting Techniques Based on Flow-induced Vibrations," *Applied Energy* 416 (2026): 127937.

44. L. Zhong, R. Liu, Y. Sun, et al., "A flexible piezoelectric film for fluid energy harvesting using wake-induced vibration," *Energy* 340 (2025): 139344.

45. Y. Cheng, F. Liu, Z. Guo, D. Chen, and K. Guo, "Enhanced energy harvesting in spacing optimized three-cylinder systems through coupled vortex-induced vibration and wake-induced galloping," *Energy* 347 (2026): 140391.

46. G. R. S. Assi, P. Bearman, and J. Meneghini, "On the Wake-induced Vibration of Tandem Circular Cylinders: The Vortex Interaction Excitation Mechanism," *Journal of Fluid Mechanics* 661 (2010): 365–401, https://doi.org/10.1017/S0022112010003095.

47. S. F. Li, P. Han, and J. L. Wang, "Enhanced Energy Harvesting From Wake-induced Rotation of an Extreme Light Circular Cylinder Under the Unsteady Vortices," *Ocean Engineering* 341 (2025), 122648.

48. D. L. Zhao, J. Zhou, T. Tan, et al., "Hydrokinetic Piezoelectric Energy Harvesting By Wake Induced Vibration," *Energy* 220 (2021): 119722.

49. M. Usman, A. Hanif, I.-H. Kim, and H.-J. Jung, "Experimental Validation of a Novel Piezoelectric Energy Harvesting System Employing Wake Galloping Phenomenon for a Broad Wind Spectrum," *Energy* 153 (2018): 882–889, https://doi.org/10.1016/j.energy.2018.04.109.

50. Y. Zhou and M. W. Yiu, "Flow Structure, Momentum and Heat Transport in a Two-tandem-cylinder Wake," *Journal of Fluid Mechanics* 548 (2006): 17–48, https://doi.org/10.1017/S002211200500738X.

51. X. H. Xue, C. Chen, Y. M. Feng, et al., "Advanced Aerodynamic Energy Harvester Based on the Dual-Cylinder Vortex-Induced Vibration Coupling Effect," *Advanced Energy Materials* 15 (2025): 02840.

52. H. Y. J. Jung, H. Ouro-Koura, A. Salalila, M. Salalila, and Z. D. Deng, "Frequency-multiplied Cylindrical Triboelectric Nanogenerator for Harvesting Low Frequency Wave Energy to Power Ocean Observation System," *Nano Energy* 99 (2022): 107365.

53. S. L. Zhang, M. Y. Xu, C. L. Zhang, et al., "Rationally Designed Sea Snake Structure Based Triboelectric Nanogenerators for Effectively and Efficiently Harvesting Ocean Wave Energy With Minimized Water Screening Effect," *Nano Energy* 48 (2018): 421–429.

Supporting Information

Additional supporting information can be found online in the Supporting Information section.

Supporting File 1: adfm77518-sup-0001-SuppMat.docx.

Supporting File 2: adfm77518-sup-0002-VideoS1-S4.zip.

16163028, 2026, 71, Downloaded from https://advanced.onlinelibrary.wiley.com/doi/10.1002/adfm.77518 by Beihang University (Buaa), Wiley Online Library on [23/09/2026]. See the Terms and Conditions (https://onlinelibrary.wiley.com/terms-and-conditions) on Wiley Online Library for rules of use; OA articles are governed by the applicable Creative Commons License